Int. J. Nav. Archit. Ocean Eng. (2013) 5:513~528
http://dx.doi.org/10.2478/IJNAOE-2013-0150
pISSN: 2092-6782, eISSN: 2092-6790

Fully nonlinear time-domain simulation of a backward bent duct buoy floating wave energy converter using an acceleration potential method

Kyoung-Rok Lee[1], Weoncheol Koo[2] and Moo-Hyun Kim[3]

[1]*Hyundai Heavy Industries, Korea*
[2]*School of Naval Architecture and Ocean Engineering, University of Ulsan, Korea*
[3]*Department of Civil Engineering, Texas A&M University, USA*

ABSTRACT: *A floating Oscillating Water Column (OWC) wave energy converter, a Backward Bent Duct Buoy (BBDB), was simulated using a state-of-the-art, two-dimensional, fully-nonlinear Numerical Wave Tank (NWT) technique. The hydrodynamic performance of the floating OWC device was evaluated in the time domain. The acceleration potential method, with a full-updated kernel matrix calculation associated with a mode decomposition scheme, was implemented to obtain accurate estimates of the hydrodynamic force and displacement of a freely floating BBDB. The developed NWT was based on the potential theory and the boundary element method with constant panels on the boundaries. The mixed Eulerian-Lagrangian (MEL) approach was employed to capture the nonlinear free surfaces inside the chamber that interacted with a pneumatic pressure, induced by the time-varying airflow velocity at the air duct. A special viscous damping was applied to the chamber free surface to represent the viscous energy loss due to the BBDB's shape and motions. The viscous damping coefficient was properly selected using a comparison of the experimental data. The calculated surface elevation, inside and outside the chamber, with a tuned viscous damping correlated reasonably well with the experimental data for various incident wave conditions. The conservation of the total wave energy in the computational domain was confirmed over the entire range of wave frequencies.*

KEY WORDS: Backward bent duct buoy; Numerical wave tank; Fully nonlinear; Acceleration potential; Viscous energy loss; Pneumatic chamber; Energy conservation; Oscillating water column.

INTRODUCTION

Since the 19th century, ocean wave energy has often been studied as a key renewable energy resource. Over 1000 patented wave energy take-off devices have been proposed as energy converters in the last several decades. Recently, as a specific functional structure system, an array of porous circular cylinders has been studied for use as an efficient wave energy take-off or attenuation system (Park et al., 2010). In general, wave energy take-off techniques are based on nine ideas (McCormick, 2007). One of the most practical and energy efficient concepts is the Oscillating Water Column (OWC), which is based on a pneumatic power take-off inside the chamber achieved by using specially designed air turbines, such as the Wells, Impulse, and Denniss-Auld turbines.

Corresponding author: *Weoncheol Koo*, e-mail: *wckoo@ulsan.ac.kr*

Since Masuda (1971) first proposed a commercially-available OWC device, several commercial-level fixed-type OWC plants have recently been constructed and operated successfully (Heath et al., 2000). Numerical analyses of fixed OWC systems have been performed by many researchers (Brendmo et al., 1996; Wang et al., 2002; Delaure and Lewis, 2003). However, most of these analyses were founded on linear-based numerical models. Koo and Kim (2010) recently developed a fully nonlinear time-domain model of a land-based OWC system. Their simulation included viscous energy loss from the chamber skirt and pneumatic pressure from oscillatory airflows in the chamber.

For a floating-type OWC system, Masuda et al. (1987) proposed a special type of OWC, a Backward Bent Duct Buoy (BBDB), which is thought to be one of the most energy-efficient OWC devices. The BBDB has the typical characteristics of dynamic behavior due to its unique body shape, such as a reverse time-mean drift force. Therefore, many studies on the hydrodynamic behaviors of BBDBs, including reverse drifting, have been conducted, either numerically or experimentally (McCormick and Sheehan, 1992; Hong et al. 2004a; 2004b; Kim et al., 2006; 2007; Nagata et al., 2008; 2009; Imai et al., 2009; Toyota et al., 2008; 2009). Suzuki et al. (2011) performed a numerical investigation to determine the optimal two-dimensional (2D) hull design of the BBDB using the eigen-function expansion method, with the relevant experiment being conducted by Toyota et al. (2010). Using a 2D numerical wave tank (NWT) technique, Koo and Lee (2011) and Koo et al. (2012) calculated the hydrodynamic behavior of a BBDB and chamber free surfaces with different shaped-corners. A proper viscous damping coefficient was applied to their numerical model, which was deducted from the experimental results.

In this study, a state-of-the-art 2D fully-nonlinear NWT technique was fully described for a simulation of a floating OWC wave energy converter, a BBDB. Using the acceleration potential method associated with pneumatic pressured chamber and viscous energy loss, the hydrodynamic performance of the floating BBDB was simulated in the time domain. The developed NWT technique was based on the potential-fluid theory and the boundary element method with constant panels on the boundaries, on which fully nonlinear free-surface and moving body boundary conditions were applied. A mixed Eulerian-Lagrangian (MEL) scheme was used for a time-varying nonlinear free-surface treatment, along with the Runge-Kutta fourth-order time integration scheme, as a time-marching approach. To accurately predict the time derivative of the velocity potential for the freely floating BBDB, the mode decomposition scheme combined with the acceleration potential was implemented to calculate the body force and displacement by simultaneously solving the equations of body motion and the velocity potential.

In order to consider the effect of pneumatic pressure acting on the free-surface inside the chamber, the damped free surface condition was applied to the NWT technique, which was first presented by Evans (1982), Sarmento and Falcao (1985) and Falnes and McIver (1985). A linear relation between the chamber pressure and airflow velocity at the air duct, as observed in various experiments, was used to model the OWC chamber (Gato and Falcao, 1988; Suzuki and Arakawa, 2000). The time-varying pneumatic pressure, due to instantaneous airflow velocity interacting with free-surface fluctuation, was numerically modeled in an OWC system. The energy loss due to viscous flow at the entrance of the BBDB hull, which could be amplified by the body motions, was also modeled by imposing an artificial viscous damping coefficient upon the free surface inside the chamber. In the potential flow calculation, the viscous damping coefficient can be obtained by a comparison of the experimental data in open chamber conditions, which represents no pneumatic chamber pressure. The difference of chamber free surface elevation between the potential-fluid-based numerical results and the experimental data in open chamber conditions can be interpreted as the viscous damping.

MATHEMATICAL FORMULATION

Boundary value problem for a floating BBDB

In order to simulate a freely floating BBDB associated with a pneumatic chamber and viscous damping, the mixed boundary value problem has to be solved using proper boundary conditions. The boundaries on the computational domain are the free surfaces inside and outside of the chamber, the body surface, the incident wave boundary, the rigid sea bottom, and the rigid end-wall. Using the velocity potential (ϕ) and a continuity equation that satisfied the entire fluid domain, the Laplace equation (Eq. (1)) was chosen as a governing equation under the assumption of inviscid, incompressible, and irrotational flows. However, a special damping can be applied on the free surface inside the chamber to represent the viscous energy loss due to body shape and motion. Using the Green function (G), the Laplace equation can be transformed into a boundary integral equation (Eq. (2)) that is solved with the corresponding boundary conditions on the respective boundaries:

$$\nabla^2\phi = 0 \tag{1}$$

$$\alpha\phi_i = \iint_{\Omega}(G_{ij}\frac{\partial\phi_j}{\partial n} - \phi_j\frac{\partial G_{ij}}{\partial n})ds \tag{2}$$

where $G_{ij}(x_i, z_i, x_j, z_j) = -(1/2\pi)\ln R_1$ for a 2D problem, the solid angle α is 0.5 for this study, and R_1 is the distance between the source (x_j, z_j) and the field points (x_i, z_i) on the boundary of the entire fluid domain.

The rigid sea bottom and the vertical end-wall of the computational domain can be described by applying a no-penetration condition so that the water particle velocity in the normal direction is zero on the rigid boundary.

$$\frac{\partial\phi}{\partial n} = 0 \tag{3}$$

The moving body boundary condition can be expressed by the fact that the water particle velocity adjacent to the body surface is the same as the body velocity in the normal direction:

$$\frac{\partial\phi}{\partial n} = V_B \cdot \vec{n} \tag{4}$$

where V_B is the body velocity at the center of gravity. When the body is stationary ($V_B = 0$), Eq. (4) becomes the rigid boundary condition. For incident waves, an analytic linear incident wave profile (Eq. (5)) was fed on the left vertical input boundary.

$$\frac{\partial\phi}{\partial n} = n_x\frac{\partial\phi}{\partial x} = n_x\frac{gAk}{\omega}\frac{\cosh k(z+h)}{\cosh kh}\cos(kx-\omega t) \tag{5}$$

where *A*, ω, *k*, and *h* are the wave amplitude, frequency, wave number, and water depth, respectively. The linear incident wave profile can be simply replaced by Stokes' 2nd-order wave profile in the case of higher wave steepness. Fully nonlinear dynamic and kinematic free-surface boundary conditions are described as:

$$\frac{\partial\phi}{\partial t} = -g\eta - \frac{1}{2}|\nabla\phi|^2 - \frac{P_a}{\rho}, \quad \frac{\partial\phi}{\partial z} = \frac{\partial\eta}{\partial t} + \nabla\phi\cdot\nabla\eta \tag{6}$$

where η is the free-surface elevation and P_a is the air pressure on the free-surface, which is set to zero (atmospheric pressure) outside the chamber. However, the pneumatic pressure should be imposed inside the chamber when the air duct is installed.

The mixed Eulerian-Lagrangian (MEL) approach was adopted to capture time-varying nonlinear free-surfaces, by which the free-surface boundary conditions can be modified using the total time derivative ($\delta/\delta t = \partial/\partial t + \vec{v}\cdot\nabla$). Since the node on the free surface was designed to follow the water particle velocity ($\vec{v} = \nabla\phi$, material-node approach and $\vec{v}$ is node velocity), the fully nonlinear free-surface boundary conditions were transformed in the Lagrangian frame:

$$\frac{\delta\phi}{\delta t} = -g\eta - \frac{1}{2}|\nabla\phi|^2 + \nabla\phi\cdot\vec{v} - \frac{P_a}{\rho} \quad \rightarrow \quad \frac{\delta\phi}{\delta t} = -g\eta + \frac{1}{2}|\nabla\phi|^2 - \frac{P_a}{\rho}$$

$$\frac{\delta\eta}{\delta t} = \frac{\partial\phi}{\partial z} - (\nabla\phi - \vec{v})\cdot\nabla\eta \quad \rightarrow \quad \frac{\delta\vec{x}}{\delta t} = \nabla\phi \tag{7}$$

where $\vec{x}$ is the node location (*x, z*). A Runge-Kutta 4th-order (RK4) scheme was used to integrate the time-dependent free surface boundary conditions (so-called time-marching) in order to obtain the velocity potential (ϕ) and surface elevation (η) at every time step.

During the nonlinear time-domain simulation, nodes on the floating body and the free surfaces must be updated and rearranged using a re-gridding scheme to avoid the numerical instability caused by the local accumulation of material nodes on the surface. The re-gridding process was carried out at every time step for a robust time-domain simulation. An artificial damping zone, as a numerical beach, was placed near the end of the fluid domain to absorb the transmitted waves and to prevent the reflected waves at the end wall. The damping coefficients were applied to both the dynamic and kinematic free surface boundary conditions (Eq. (8)).

$$\frac{\delta\phi}{\delta t} = -g\eta + \frac{1}{2}|\nabla\phi|^2 - \frac{P_a}{\rho} - \mu_1\frac{\partial\phi}{\partial n}, \quad \frac{\delta\eta}{\delta t} = \frac{\partial\phi}{\partial z} - \mu_2\eta \tag{8}$$

where μ_1 and μ_2 are damping coefficients, whose values are properly selected depending on the wave conditions.

A frontal damping zone was also installed on the free surface in front of the incident wave boundary to prevent a re-reflection at the wave maker, which enables long time simulation of surface-piercing bodies. This special damping scheme has to be designed so as to suppress only the reflected waves from the floating body, while preserving the original incident waves. In this regard, the adopted damping term should be applied to the difference between the total waves and incident waves. Then, the free surface boundary conditions can be expressed as:

$$\frac{\delta\phi}{\delta t} = -g\eta + \frac{1}{2}|\nabla\phi|^2 - \frac{P_a}{\rho} - \mu_{1f}\left(\frac{\partial\phi}{\partial n} - \frac{\partial\phi}{\partial n}*\right), \quad \frac{\delta\eta}{\delta t} = \frac{\partial\phi}{\partial z} - \mu_{2f}(\eta - \eta*) \tag{9}$$

where μ_{1f} and μ_{2f} are the frontal damping coefficients for absorbing the reflection waves from the body, and the reference values of $(\partial\phi/\partial n)*$ and $\eta*$ were computed using the same computational conditions in the absence of bodies. For the case of moderate nonlinear incident waves, proper analytic solutions (e.g., second-order Stokes waves) can be used in the practical applications, as determined by Tanizawa and Naito (1997). For the efficient absorption of wave energy, a spatial ramp function was applied to the selected damping coefficients (μ_1, μ_2 and μ_{1f}, μ_{2f}) over the damping zone of two wavelengths (2 λ). The direction of the ramp to the target value in the frontal damping is opposite to the case of rear damping zone. In the present study, open sea conditions can be realized in the computational domain by using both the frontal damping and the numerical beach.

A temporal ramp function at the input boundary was applied during the first two wave periods (2T) to prevent the impulse-like behavior of the wave maker and to reduce the corresponding unnecessary transient waves. A Chebyshev five-point smoothing scheme was used along the free surface during the time integration to avoid the non-physical, saw-tooth numerical instability on a highly nonlinear free surface. The smoothing scheme was applied at every fifth time step for a stable time simulation. More detailed explanations of the general numerical schemes and formulations in the NWT technique are given in a previous study (Koo and Kim, 2004).

OWC chamber modeling associated with power take-off and viscous damping

The time-varying pneumatic pressure caused by the oscillating water column can be described as the rate of change of air volume inside the chamber (Kim and Iwata, 1991). The rate of air volume change is also directly related to the relative spatial-mean vertical velocity between the body and free surface inside the chamber. The pneumatic pressure in the chamber at each time step is expressed as (Koo and Lee, 2011; Koo et al., 2012):

$$P_{ac}(t) = \frac{C_{dm}\Delta V}{A_d\Delta t} = C_{dm}U_d(t) \tag{10}$$

where C_{dm} is an equivalent linear pneumatic coefficient determined by the air duct-chamber area ratio, $\Delta V/\Delta t = (V_t - V_{t-\Delta t})/\Delta t$

is the time-differential change of air volume in the chamber (V_t is the volume at the current time step, while $V_{t-\Delta t}$ is the volume at the previous time step), A_d is the sectional area of the air duct, and $U_d(t)$ is a time-varying airflow velocity at the air duct under the assumption of incompressible air in the case of a relatively large air opening. Sarmento and Falcao (1985) pointed out the spring-like effects, due to air compressibility in the OWC chamber, for a relatively large air volume compared with a small nozzle outlet, which was not considered in the present analysis. Therefore, the case of this study can represent the large-diameter air turbine system, such as Wells turbine and Impulse turbine. Koo and Kim (2010) also studied pneumatic pressure formulation and its application to a fixed OWC chamber.

In addition to pneumatic pressure, a pressure drop induced by viscous energy loss occurs inside the chamber because a viscous-flow phenomenon, such as vortex shedding, arises at the corner of the BBDB. When the piston-like movement of chamber surface elevation occurs, as in a case of resonance frequencies, and the ensuing high velocity flows are generated, the magnitude of the viscous energy loss greatly increases. In this regard, the difference in the chamber surface elevation between the potential-flow-based numerical solutions and the experimental results can be interpreted as viscous energy loss (work done). A typical entry pressure drop ($\Delta P = K_L \frac{1}{2}\rho V^2$), where K_L is the loss coefficient and V is the flow velocity, can be linearized, so that the flow velocity is proportional to the vertical velocity of the water column ($V \approx \partial\eta/\partial t = \dot{\eta}$). Then, the pressure drop in the chamber can be described as (Koo and Kim, 2010):

$$P_v(t) = K_L^* \bar{\dot{\eta}}(t) = \nu \frac{\partial \phi(t)}{\partial n} \tag{11}$$

where K_L^* denotes a modified energy loss coefficient, $\bar{\dot{\eta}}$ represents the time-varying spatial-mean surface velocity inside the chamber, and ν is an equivalent linear viscous damping coefficient.

Generally, the pneumatic pressure and viscous energy loss are approximately proportional to the square of the airflow velocity and water column velocity, respectively. Hence, Eqs. (10) and (11), which have an equivalent linear coefficient, can be modified to equations with a quadratic coefficient. The quadratic pneumatic (P_{ac}) and viscous-loss pressure drop (P_v) can be applied straightforwardly to the present nonlinear time-domain simulation:

$$P_{ac}(t) = D_{dm} U_d(t) \left| U_d(t) \right| \quad , \quad P_v(t) = \nu_q \frac{\partial \phi(t)}{\partial n} \left| \frac{\partial \phi(t)}{\partial n} \right| \tag{12}$$

where D_{dm} and ν_q denote the quadratic pneumatic and viscous-loss coefficients, respectively. Therefore, the final dynamic free-surface boundary conditions inside the chamber (including an equivalent linear or quadratic pneumatic pressure and viscous pressure drop) can be expressed, respectively, as:

$$\frac{\delta \phi}{\delta t} = -g\eta + \frac{1}{2}\left|\nabla \phi\right|^2 - \frac{1}{\rho}\left(C_{dm} U_d + \nu \frac{\partial \phi}{\partial n} \right) \quad \text{or} \quad \frac{\delta \phi}{\delta t} = -g\eta + \frac{1}{2}\left|\nabla \phi\right|^2 - \frac{1}{\rho}\left(D_{dm} U_d \left| U_d \right| + \nu_q \frac{\partial \phi}{\partial n} \left| \frac{\partial \phi}{\partial n} \right| \right) \tag{13}$$

Energy conservation of the BBDB system

The BBDB system contains five energy-flux components: input, reflection, transmission, energy extraction by airflow, and energy loss by viscosity. The transferred wave energy flux into the energy converter is proportional to the square of the wave height and the wave group velocity. Outside the chamber, the energy-flux components per unit area are expressed as:

$$E_i C_g = \frac{1}{8}\rho g H_i^2 C_g, \quad E_R C_g = \frac{1}{8}\rho g H_R^2 C_g, \quad E_T C_g = \frac{1}{8}\rho g H_T^2 C_g \tag{14}$$

where C_g is the wave group velocity, and H_i, H_R, and H_T represent the incident, reflected, and transmitted wave heights, respectively. E_i, E_R, and E_T also denote the respective energy components. Inside the chamber, the available pneumatic po-

wer in Watts (*AP*) and the rate of energy dissipation (*DR*) based on the linear (or quadratic) coefficients can be simplified as (Koo and Kim, 2010):

$$AP = \frac{1}{2} C_{dm} A_d U_0^2 \ (\text{or } \frac{4}{3\pi} D_{dm} A_d U_0^3) \quad , \quad DR = \frac{1}{2} \nu B_{dm} V_0^2 \ (\text{or } \frac{4}{3\pi} \nu_q B_{dm} V_0^3) \tag{15}$$

where B_{dm} is the chamber width, and V_0 is the amplitude of the relative spatial-mean vertical velocity of the free surface. Therefore, the energy conservation of the total energy flux in the BBDB system is given by:

$$\frac{1}{8} \rho g H_i^2 C_g = \frac{1}{8} \rho g H_R^2 C_g + \frac{1}{8} \rho g H_T^2 C_g + \frac{1}{2} C_{dm} A_d U_0^2 + \frac{1}{2} \nu B_{dm} V_0^2 \tag{16}$$

Acceleration potential method for a freely floating BBDB

The time derivative of the velocity potential ϕ_t is a critical value when obtaining the accurate pressure and force acting on a freely floating body, as determined by Koo and Kim (2004). The ϕ_t on the body-surface node has to be obtained by simultaneously solving the fluid particle and body motion equations. Thus, the use of the acceleration potential method for obtaining ϕ_t is the most accurate and consistent way to predict the motion of a freely floating body. The wave force on a floating body can be calculated by integrating Bernoulli's pressure over the instantaneous wetted body surface. Including the gravitational and external restoring spring forces, if any, the total force in the *i*-th direction for a 2D body can be calculated as follows:

$$F_i = \int_{S_B} -\rho(\phi_t + \frac{1}{2}|\nabla\phi|^2 + gz) \cdot \vec{n}_i ds - Kx\delta_{i1} - C\dot{x}\delta_{i1} - W\delta_{i2} \tag{17}$$

where *K* and C represent the additional horizontal spring and damping coefficients, respectively. *x* is the surge, *z* is the heave, $\dot{x}$ is the horizontal body velocity, *W* is the weight of the body (= *mg*), δ_{ij} denotes the Kronecker delta function (horizontal, i = 1; vertical, i = 2), and S_B is the wetted body surface.

In order to implement the acceleration potential method, we used the mode decomposition method introduced by Vinje and Brevig (1981) to obtain the time derivative of the velocity potential directly from the acceleration field. In a 2D problem, the acceleration field can be decomposed into four modes, corresponding to three unit accelerations for surge-heave-pitch and the acceleration due to the velocity field. Hence, each mode can be obtained by solving the respective boundary integral equation in the acceleration field. Using these four modes and the equation of body motion, the body acceleration can be determined.

The time derivative of the velocity potential ϕ_t on a floating body for a 2D problem is given by:

$$\phi_t = \sum_{i=1}^{3} a_i \varphi_i + \varphi_4 \tag{18}$$

where a_i is the *i*-th mode component of generalized body acceleration (1 = surge, 2 = heave, 3 = pitch).

To solve the boundary integral equation for each mode in the acceleration field, the body boundary condition is given as:

$$\frac{\partial \varphi_i}{\partial n} = \begin{Bmatrix} n_i, & i = 1 \sim 3 \\ q_B, & i = 4 \end{Bmatrix} \tag{19}$$

where, $n_1, n_2,$ and n_3 denote the unit normal vector in the respective direction (1 = surge, 2 = heave, 3 = pitch), and q_B represents the contribution of the velocity field to the acceleration field, which can be written for a 2D simulation as follows (Koo and Kim, 2004):

$$\begin{aligned} q_B = {} & n_x\left[\omega_0{}^2 x_P + 2\omega_0\left(\frac{\partial\phi}{\partial z} - \upsilon_Z\right)\right] + n_z\left[\omega_0{}^2 z_P - 2\omega_0\left(\frac{\partial\phi}{\partial x} - \upsilon_X\right)\right] \\ & - k_n\left[\left(\frac{\partial\phi}{\partial x} - \upsilon_X - \omega_0 z_P\right)^2 + \left(\frac{\partial\phi}{\partial z} - \upsilon_Z + \omega_0 x_P\right)^2\right] \\ & + k_n\left[\left(\frac{\partial\phi}{\partial x}\right)^2 + \left(\frac{\partial\phi}{\partial z}\right)^2\right] + \frac{\partial\phi}{\partial n}\left(\frac{\partial^2\phi}{\partial s^2}\right) - \frac{\partial\phi}{\partial s}\frac{\partial}{\partial s}\left(\frac{\partial\phi}{\partial n}\right) \end{aligned} \tag{20}$$

where n and s are normal and tangential unit vectors of the body surface, respectively, $k_n = -1/\rho *$ is the local curvature along the s direction, x_P, z_P denote the position of point P from a body's center of gravity, and $\upsilon_{X,Z}$ and ω_0 are the translational and angular velocities of a body, respectively.

The free-surface boundary conditions for the respective free surface areas of the BBDB system in the acceleration field are also given as:

$$\varphi_4 = \begin{cases} -g\eta - \frac{1}{2}|\nabla\phi|^2 - \mu_1\left(\frac{\partial\phi}{\partial n} - \frac{\partial\phi}{\partial n}*\right), & \text{for frontal damping zone} \\ -g\eta - \frac{1}{2}|\nabla\phi|^2, & \text{for outside the chamber} \\ -g\eta - \frac{1}{2}|\nabla\phi|^2 - \frac{1}{\rho}\left(C_{dm}U_d + \nu\frac{\partial\phi}{\partial n}\right), & \text{for inside the chamber(linear chamber model)} \\ -g\eta - \frac{1}{2}|\nabla\phi|^2 - \mu_1\left(\frac{\partial\phi}{\partial n}\right), & \text{for end damping(numerical beach) zone} \end{cases} \tag{21}$$

where φ_i for i = 1~3 modes is zero for the free surface boundary conditions in the acceleration field. The input boundary and other rigid boundary conditions are given as:

$$\frac{\partial\varphi_i}{\partial n} = \begin{cases} 0, & i = 1\sim 3 \\ \frac{\partial\phi_t}{\partial n}, & i = 4 \end{cases} \text{ on input boundary}, \quad \frac{\partial\varphi_i}{\partial n} = \{0, \quad i = 1\sim 4\} \text{ on rigid boundary} \tag{22}$$

After solving the boundary integral equation in the acceleration field for the aforementioned conditions, φ_i for i = 1~4 on the body surface (Eq. (18)) is obtained. To calculate the generalized acceleration (a_i) in Eq. (18) for each mode (surge, heave, and pitch), the force equation should be combined with Newton's second law. Including the gravitational force and external force (e.g., horizontal spring), the total force and moment in the i-th direction can be calculated as follows:

$$ma_1 = F_1(=F_x) = \int_{S_B} P\, n_1 ds - Kx - C\dot{x} \tag{23}$$

$$ma_2 = F_2(=F_z) = \int_{S_B} P\, n_2 ds - W \tag{24}$$

$$Ia_3 = F_3(=M) = \int_{S_B} P\, n_3 ds \tag{25}$$

where $P = -\rho(a_1\varphi_1 + a_2\varphi_2 + a_3\varphi_3 + \varphi_4 + gz + \frac{1}{2}|\nabla\phi|^2)$, m is the body mass, I is mass moment of inertia.

From Eqs. (23) to (25), three unknown accelerations (a_i) of each mode can finally be determined. Using the Runge-Kutta-Nystrom 4th-order integration method, the body acceleration, velocities and displacements are then consecutively determined. The calculated translational and rotational body displacement is used to update the body geometry for the next time step.

In the present study, a freely floating BBDB with no additional mooring lines was used to evaluate the hydrodynamic performance. Therefore, neither horizontal spring nor damping coefficients was applied to Eq. (23). In the fully nonlinear simulation, the instantaneous position of the BBDB was updated at every time step and the body drifts during the time simulation.

EXPERIMENTAL SETUP

In order to verify the calculated results from the developed numerical model, an experiment was conducted independently in the 2D wave tank at the University of Ulsan (Koo and Lee, 2011). The wave tank dimensions were 0.5 × 0.4 × 35 *m* (width × depth × length). A flap-type wave maker and a sloped beach were positioned at both ends of the tank. Six wave probes were installed to measure surface elevations: three in the weather side, two in the lee side, and one in the middle of the chamber. The measured signals of surface elevations were amplified by the AMP and gathered into the DAQ board.

Table 1 shows the specifications of the BBDB model used in Koo and Lee (2011). Since the width of BBDB model is 0.48 m compared with the tank width (0.5 *m*), there is no side wall effect. In order to avoid friction during the body motions in a 2D wave tank, four bearings were mounted on each corner of the model along the wall of the wave tank, by which the BBDB model occupied the whole width of the tank and a three-degree-of-freedom motion can be allowed. According to the tank size and the performance of the wave maker, incident waves of periods from 0.6 *s* to 1.4 *s* with a height of 0.01 *m* were generated.

Since the wave maker used in the present experiment cannot control the reflected waves from the floating body, the re-reflection may occur when the duration of wave generation is long. Therefore, the steady-state waves with no contamination from the re-reflected waves are only used to compare the numerical results.

Table 1 Specifications of the BBDB model.

Item	
Length (*L*)	0.35 *m*
Breadth (*B*)	0.48 *m*
Model height	0.24 *m*
Draft	0.16 *m*
Displacement	0.012 m^3
Chamber width (*gap*)	0.08 *m*
Backward bent width	0.08 *m*
Body wall thickness	0.01 *m*
Radius of gyration	0.134 *m*
Center of gravity (Cx, Cz) (Cx from F.P, Cz from MWL)	(0.155 *m*, 0.109 *m*)
Total model mass	12.42 *kg*
Ballast mass for even keel	9.86 *kg*

NUMERICAL RESULTS AND DISCUSSION

A schematic diagram and coordinate system for the present numerical model is shown in Fig. 1. The flowchart of computational algorithm is also shown in Fig. 2. The dimensions of the BBDD are the same as those in the experimental model (Table 1). Each side of the free surface (weather and lee side) is four times the incident wavelength (4λ), including the artificial damping zone of the two wavelengths (2λ), to dampen the designated waves sufficiently at the end of the fluid domain. A flat

rigid sea bottom was set at a depth of 0.4 m. In order to prevent a re-reflection from the wave maker, a special damping scheme on the free surface, called the frontal damping zone (Koo and Kim, 2004) of two wavelengths (2λ), was also installed near the wave maker zone. From the convergence test for various node numbers and time step intervals (Fig. 3), 20 nodes (or more) per incident wavelength and a time step of $dt = T / 64$ (or less) interval were used to produce the numerical results.

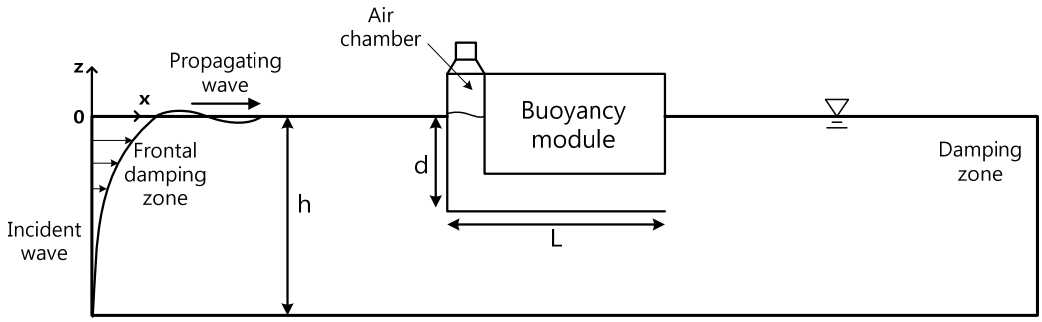

Fig. 1 Overview of computational domain.

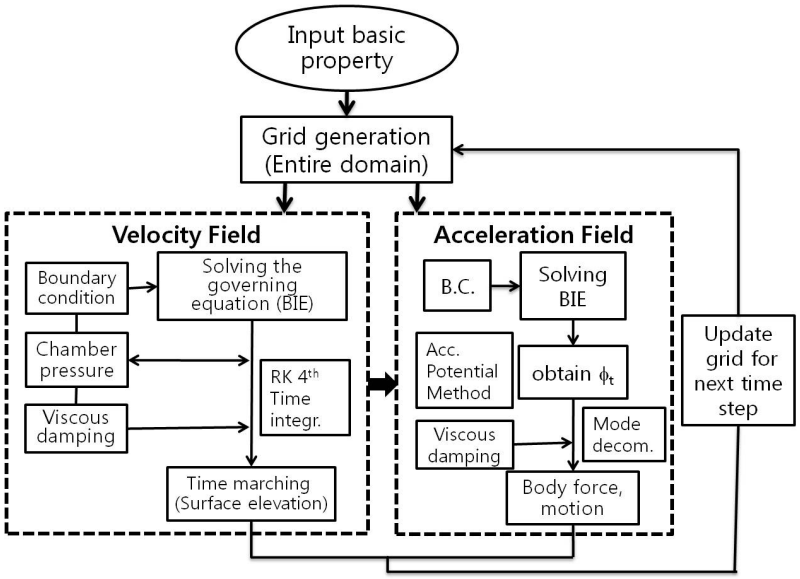

Fig. 2 Flowchart of the computational algorithm.

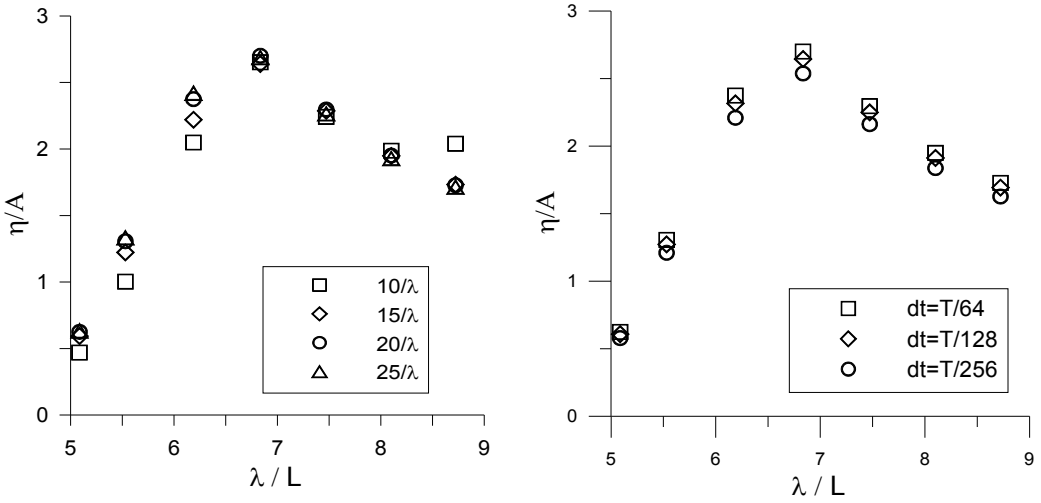

Fig. 3 Convergence test for node number and time segment (comparison of surface elevation inside the chamber).

Initially, the calculated wave elevations of the fixed BBDB were compared with the experimental data (Fig. 4) to determine the viscous energy loss due to the body shape. The linear and nonlinear results were also compared to evaluate the effect of nonlinear interactions between wave and body. A significant difference was observed between the numerical and experimental results near the resonance frequencies, where the incident wavelength was approximately six times greater than the total body length (L). Some discrepancy between numerical results and experimental data was also found at longer wavelength ($\lambda / L > 8$), which may be due to a measurement error at the tank experiment and the effect of wave reflection at the end-wall of the physical wave tank installed with wave absorbing material. In general, it is difficult to fully control the wave reflection at the downstream of the tank when the incident wave is longer than a certain limitation of the tank capacity. The wave tank used in this study does not have a sufficient capacity of wave absorbing system at the downstream.

Since a small incident wave steepness was applied to the entire frequency range ($0.00243 < H / \lambda < 0.0131$, H = 0.01 m), there was little difference between the linear and nonlinear results. When the incident wave becomes higher (H = 0.02 m and 0.04 m) in the nonlinear calculation, the chamber surface elevation does not change much compared to the case of H = 0.01 m, which implies that the effect of wave nonlinearity is not significant in the fixed body. Since this study is mainly focused on the development of numerical tool to simulate a floating OWC system, BBDB and to validate the numerical results compared with the experiment, the numerical simulation with large waves and the violent body motions will be studied as the next research topic.

The discrepancy between the numerical and experimental results in the resonance frequency was caused by viscous loss. Energy loss due to vortex generation may occur at the sharp corners of the BBDB.

In order to compensate for the viscous energy loss with the artificial damping in the fixed BBDB system, a small viscous damping coefficient ($\nu = 0.09$) was applied to the free-surface boundary inside the chamber (Fig. 5). The damping coefficient chosen matched the experimental results in the open chamber condition, where the difference between the numerical results and experimental data was caused by viscous energy loss. The viscous damping coefficient was divided by the water density (ρ = 1000). Fig. 4 shows a comparison of surface elevations with applications of viscous damping on the free surface. Due to the relatively narrow chamber, compared to wavelength, the pumping mode of the free surface elevation was observed over the whole range of frequencies. The simulated elevations with a chosen viscous damping coefficient were in agreement with the experimental values. The applied damping coefficient only affected the resonance frequency region, with the other regions being only minimally affected.

A comparison of surface elevations at the weather and lee sides is shown in Fig. 6. All data were measured at 1 m ahead of the body. The calculated elevations, with a tuned viscous coefficient ($\nu = 0.09$), were in good agreement with the experimental

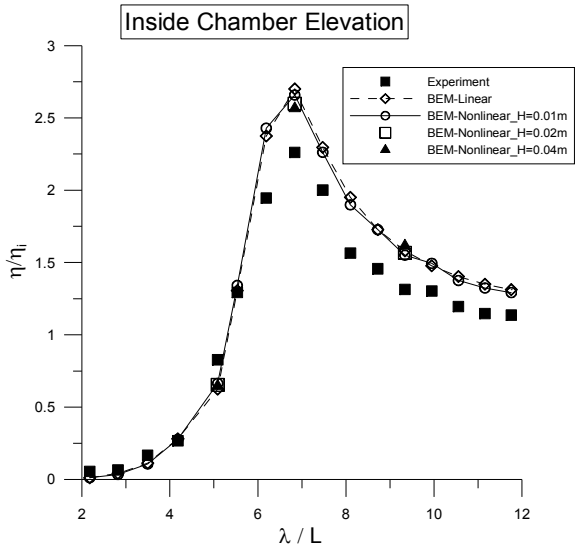

Fig. 4 Comparison of open chamber elevations for the experimental, linear and nonlinear calculations of the fixed body case (H = 0.01, 0.02, 0.04 m).

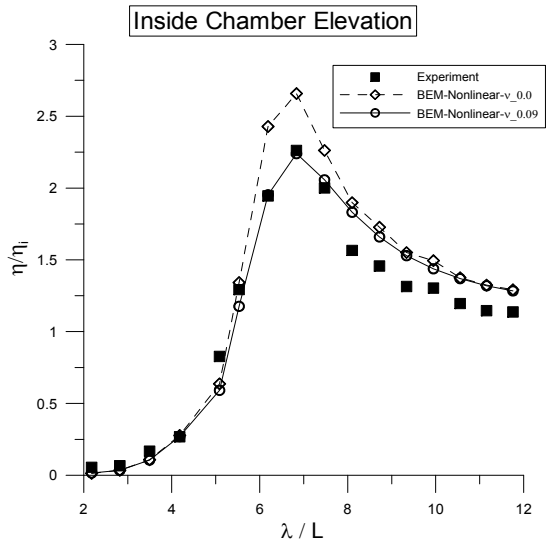

Fig. 5 Comparison of open chamber elevations of the experimental and nonlinear calculations for the case of a fixed body (H = 0.01 m).

results. It is also observed that a slight difference between the cases of viscous damping and no damping, which implies that the effect of a small viscous damping coefficient ($\nu = 0.09$) on the free surface elevation outside the chamber is not significant. Since a reflected wave cannot be controlled in the experiment, especially in the case of a surface piercing body, a slight deviation can be found between the two results in the weather side. The linear and nonlinear calculations were similar, because of the small incident wave steepness (similar to the effect seen in Fig. 4).

Total energy conservation of the fixed BBDB system is compared in Fig. 7. For the open chamber conditions ($C_{dm} = 0$), the sum of the three energy fluxes of reflection, transmission, and viscous energy loss was equal to the incident wave energy flux. In the case of the pneumatic chamber ($C_{dm} = 0.7$), the sum of all of the energy components, including the pneumatic energy due to air flow, was conserved over the whole range of frequencies. Comparing the respective energy components showed that the total energy of the fixed BBDB system was conserved in the computational domain during the time simulation. A small discrepancy was observed in the shorter wave length, which may be due to the numerical measurement of large reflected waves in front of BBDB, with an insufficient number of probes on the free surface.

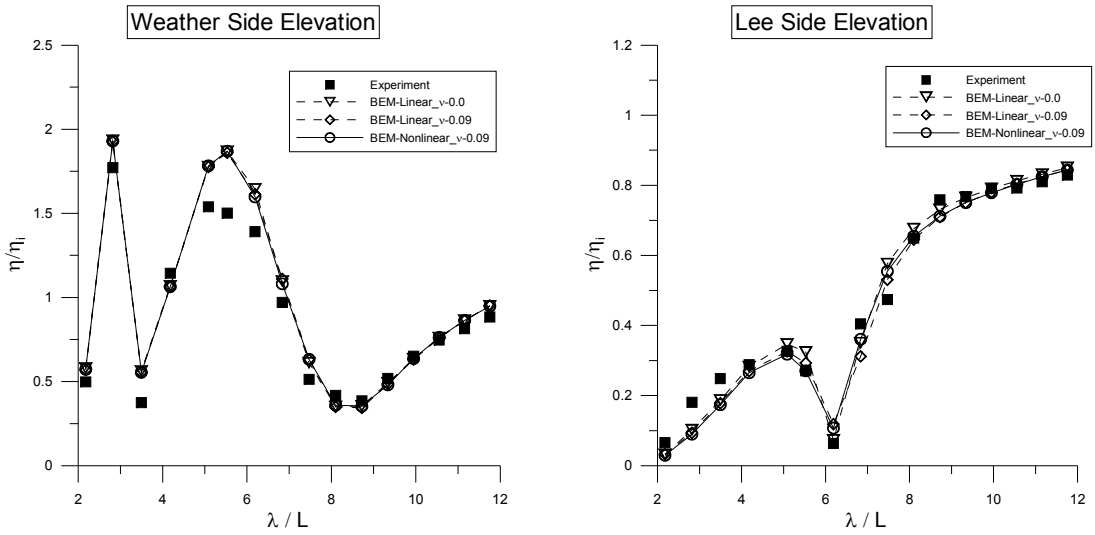

Fig. 6 Comparison of wave elevations for the experimental, linear and nonlinear calculations with a viscous damping coefficient (($\nu = 0.09$) for the fixed body case (H = 0.01 *m*).

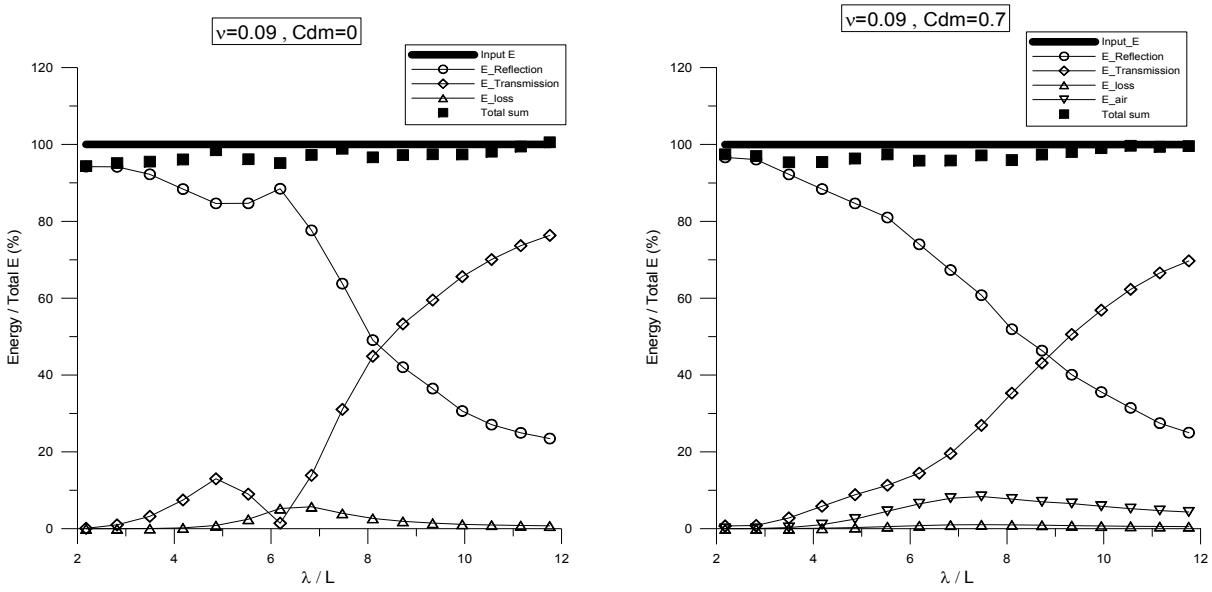

Fig. 7 Comparison of energy components with a viscous damping coefficient ($\nu = 0.09$) and energy extraction ($C_{dm} = 0.7$) in the fixed body case.

For the floating BBDB system, Fig. 8 shows the comparison of chamber surface elevations for the experimental and numerical calculations. With a tuned linear equivalent viscous damping coefficient ($\nu = 0.52$), the nonlinear calculation was in agreement with the experimental data, which was also determined by Koo and Lee (2011). With a quadratic viscous damping coefficient ($\nu_q = 13$), the calculated results also matched the cases of the linear damping coefficient and experimental data. Practically, there is no fundamental difference between the use of a linear viscous damping and a quadratic viscous damping during the present simulation, because a proper damping coefficient can be obtained from the experiment. In this study, the comparison of the damping effect between the linear and quadratic coefficients was evaluated and the characteristics of the results were investigated. More detailed studies on the effect of viscous damping type, its proper selection from various experimental data, and the general application of the damping coefficients should be conducted as the next research topics.

The proper viscous damping can be obtained from a comparison of the experimental data with the open chamber conditions, where the viscous energy loss only exists without pneumatic pressure. The viscous damping coefficients shown in the figures were divided by water density (($\rho = 1000$). The incident wave height of 0.01 *m* was used for the linear calculation, whereas the height of 0.005 *m* was chosen for nonlinear calculation, so as to prevent numerical instability attributed to the extreme nonlinear body motions near the resonance frequencies. Compared with the fixed BBDB case, the deviation between the experimental and numerical results without viscous damping is significant near the resonance frequencies ($\lambda / L \approx 4.5 \sim 5.0$). Thus, it can be inferred that viscous energy loss may greatly increase due to the motion of the BBDB. In particular, the pitch of the BBDB could intensify the vortex generation at the corner of the body.

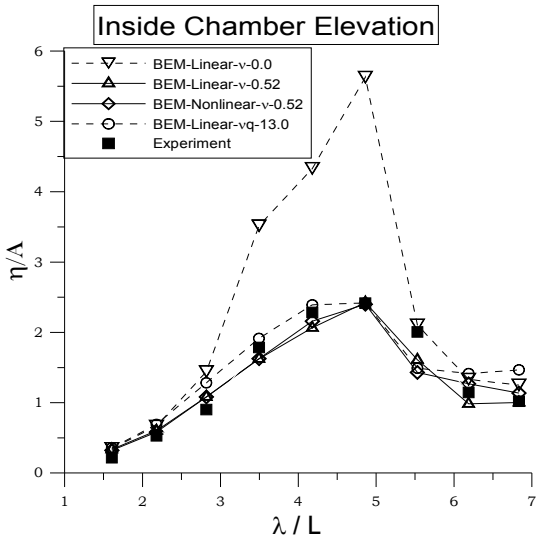

Fig. 8 Comparison of open chamber surface elevations for experimental and numerical calculations with either a linear ($\nu = 0.52$) or a quadratic ($\nu_q = 13.0$) viscous damping coefficient in the case of a freely floating BBDB.

Fig. 9 shows a comparison of the surface elevations at the weather and lee sides of the BBDB with the application of a linear viscous damping coefficient inside the chamber free surface. The calculated elevations agree reasonably well with those from the experimental data. Due to the difficulty in controlling the reflected waves in the floating body experiment, the measured elevations deviate from the numerical results at some frequencies, especially in the long wave region. Since a relatively large motion of the BBDB magnifies the radiated waves, the nonlinear calculation results with updated body and free-surface motions showed greater accuracy than the linear results calculated with a mean-positioned body and free surface. The magnitude of elevation at the lee side is smaller near the resonance frequency region ($\lambda / L \approx 4.5 \sim 5.0$) than at the other frequencies. This phenomenon can be explained by the fact that a greater portion of incident wave energy is damped by viscosity-induced loss due to high vertical flow velocities, as well as large body motions. Thus, the transmitted wave energy becomes small. As mentioned earlier, a slight discrepancy of the total energy between the input and total summated energy may be due to an insufficient number of wave probes during the numerical measurement on the free surface including numerical aliasing error.

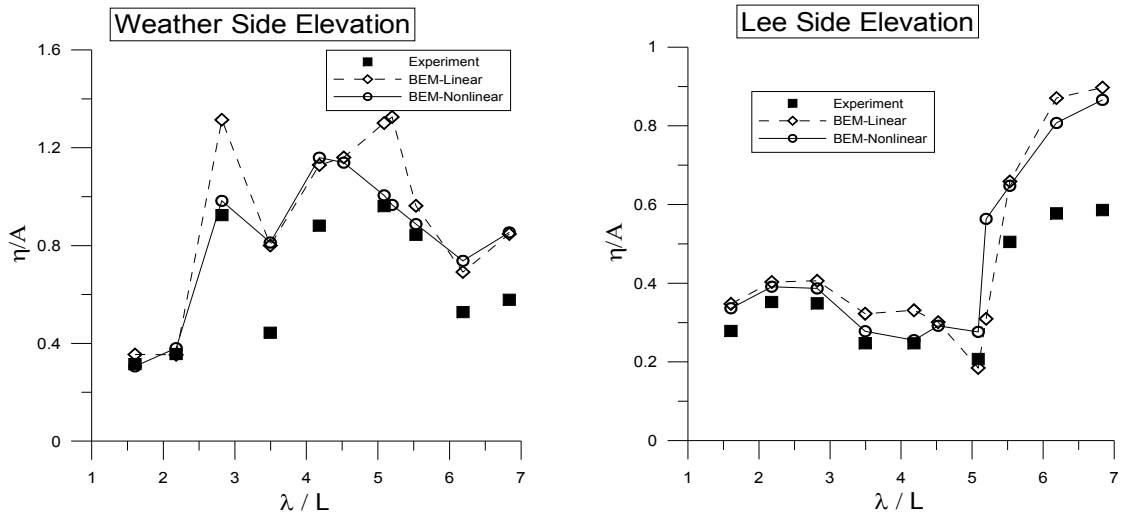

Fig. 9 Comparison of wave elevations outside the camber in the case of a freely floating BBDB with a linear equivalent damping coefficient ($\nu = 0.52$) (Koo and Lee, 2011).

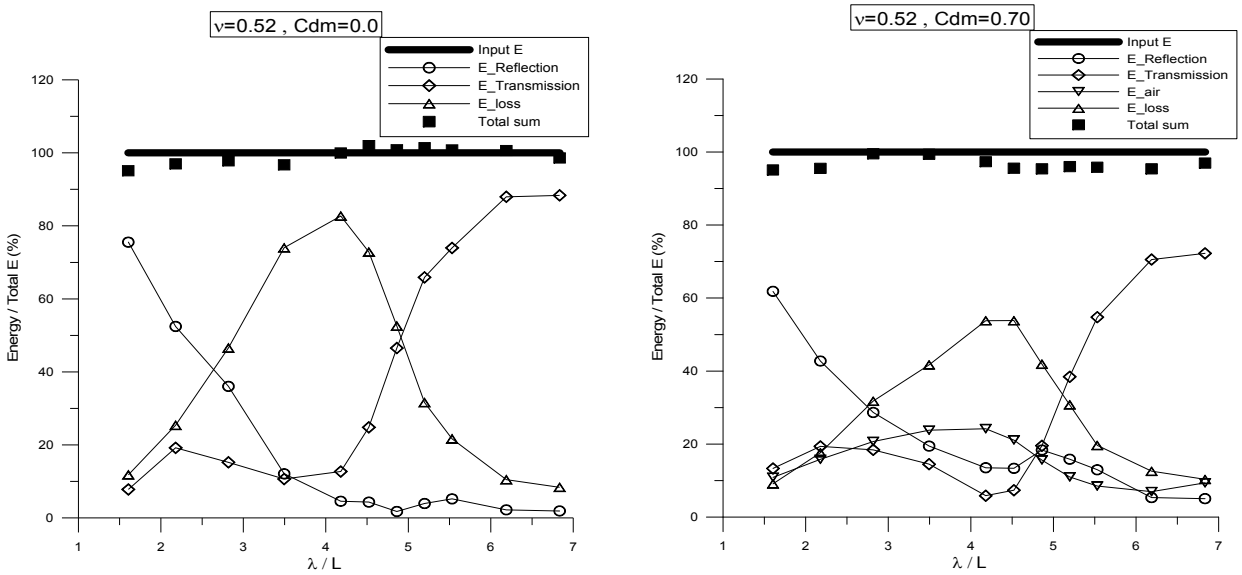

Fig. 10 Comparison of energy components of the freely floating BBDB with viscous damping coefficient (($\nu = 0.52$) and open chamber ($C_{dm} = 0.0$) and pneumatic chamber conditions ($C_{dm} = 0.7$).

The respective energy components of the floating BBDB for both chamber conditions are compared in Fig. 10. In the open chamber conditions (left graph), as pointed out by Koo and Lee (2011), the relative energy loss by viscosity near the resonance frequencies is up to 80% of the incident wave energy, which indicates that a large amount of energy could be lost at the sharp corners of the body by the resonant pitch-induced vortices. In the pneumatic chamber conditions (right graph), the relative energy loss can be reduced by 50% of the total energy. This can be explained by the fact that the motion of the BBDB decreesed due to the effect of the pneumatic pressured chamber, resulting in a diminished vortex generation. In both chamber conditions, the total energy in the computational domain was conserved over the whole range of frequencies. Comparing with Fig. 7, the magnitude of the pneumatic energy in the floating case (about 25% of incident energy) was greater than that in the fixed case (about 10%). Thus, the body motion (heave and pitch) may amplify the relative vertical water column velocity, thus increasing the resultant airflow velocity.

A comparison of the available wave power with various pneumatic coefficients (C_{dm}) is shown in Fig. 11. As the coefficient increases, indicating that the ratio of chamber surface area to air duct area increases, the airflow velocity at the nozzle

outlet increases until the air opening is relatively large, under the assumption of incompressible air. The maximum available pneumatic power can be found near the resonance frequencies.

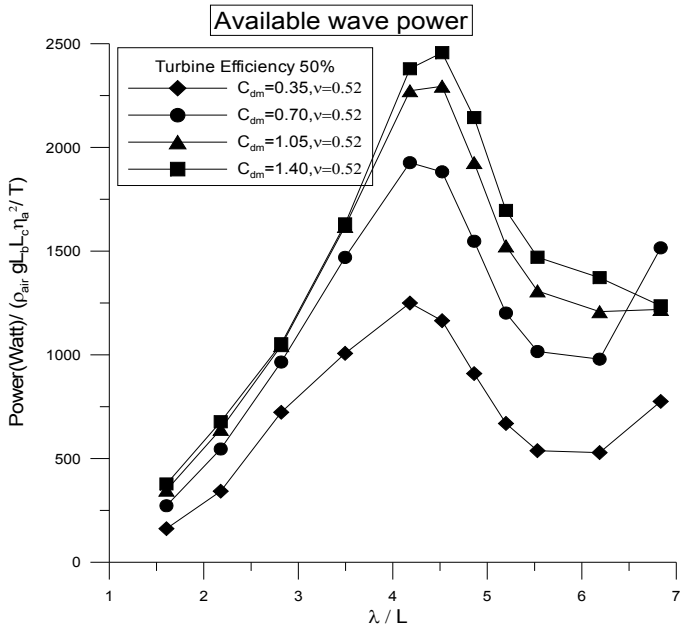

Fig. 11 Comparison of available wave power with various extraction coefficients.

CONCLUSIONS

The hydrodynamic performance of a floating OWC device was evaluated in the time domain. An acceleration potential method using full-updated matrix calculation, associated with a mode decomposition scheme, was implemented to obtain the hydrodynamic force and displacement of a freely floating BBDB. The developed NWT technique was based on the potential theory and the boundary element method with constant panels on the boundaries, on which fully nonlinear free-surface and moving-body boundary conditions associated with OWC power take-off were applied. The modeling of the pneumatic chamber and viscous damping was proportional to the square of the airflow velocity and water column velocity, respectively. However, the numerical model can also be simplified to a linear relation. Open sea conditions can be realized in the computational domain by using the frontal damping and the numerical beach. Therefore, the NWT technique was better than the experiment in controlling the reflected waves from the wave maker and floating body.

A significant difference of chamber surface elevation was observed between the numerical and experimental results near the resonance frequencies, which may be attributed to the viscous energy loss. The energy loss by vortex generation may increase at the sharp corners of the BBDB. The numerical results under the open chamber conditions were adjusted by adding a proper viscous damping coefficient, obtained from a comparison of the experimental data. The calculated surface elevations affected by pneumatic pressure correlated reasonably well with the experimental values.

The total energy summation of the BBDB system in the computational domain was found to be conserved over the whole range of frequencies. In the case of a floating BBDB with an open chamber, the relative energy loss due to viscosity near the resonance frequencies was up to 80% of the incident wave energy, which indicates that a large amount of energy could be lost at the sharp corners of the body by the resonant pitch-induced vortices.

Since a relatively large motion of the BBDB magnified the radiated waves, the nonlinear results that were calculated using the updated free-surface and body motions were found to be more accurate than the linear ones with a mean-positioned free surface and body.

The developed NWT model for a floating BBDB device can be used to analyze the hydrodynamic performance of a floating-type OWC system. Using a parametric study for various conditions compared with the corresponding experiments, it is possible to predict the motion characteristics and determine the proper BBDB shape for various environmental conditions.

REFERENCES

Brendmo, A., Falnes, J. and Lillebekken, P.M., 1996. Linear modelling of oscillating water columns including viscous loss. *Applied Ocean Research,* 18(2), pp.65-76.

Delaure, E.M.C. and Lewis, A., 2003. 3D hydrodynamic modelling of fixed oscillating water column wave power plant by a boundary element methods. *Ocean Engineering,* 30(3), pp.309-330.

Evans, D.V., 1982. Wave power absorption by systems of oscillating surfacepressure distributions. *Journal of Fluid Mechanics*, 114, pp.481-499.

Falnes, J. and McIver, P., 1985. Surface wave interactions with systems of oscillating bodies and pressure distributions. *Applied Ocean Research*, 7(4), pp.225-234.

Gato, L.M.C. and Falcão, A.F.O., 1988. Aerodynamics of the wells turbine. *International Journal of Mechanical Science,* 30, pp.383-395.

Heath, T., Whittaker, T.J.T. and Boake, C.B., 2000. The design, construction and operation of the LIMPET wave energy converter. *Proceedings of 4th European Wave Energy Conference*, Aalborg, Denmark, 4-6 December 2000, pp.49-55.

Hong, D.C., Hong, S.Y. and Hong, S.W., 2004a. Numerical study of the motions and drift force of a floating OWC device. *Ocean Engineering*, 31(2), pp.139-164.

Hong, D.C., Hong, S.Y. and Hong, S.W., 2004b. Numerical study on the reverse drift force of floating BBDB wave energy absorbers. *Ocean Engineering*, 31(10), pp.1257-1294.

Imai, Y., Toyota, K., Nagata, S., Setoguchi, T., Oda, J., Matsunaga, N., Manago, Y. and Shimozono, T., 2009. Experimental study on negative drift force acting on a floating OWC-type wave energy converter "Backward Bent Duct Buoy". *Proceedings of 19th International Offshore and Polar Engineering Conference*, ISOPE, Osaka, Japan, 21-26 June 2009, pp.331-338.

Kim, D. and Iwata, K., 1991. Dynamic behavior of tautly moored semi-submerged structure with pressurized air-chamber and resulting wave transformation. *Coastal Engineering in Japan,* 34(2), pp.223-242.

Kim, J.H., Lew, J.H., Hong, D.C. and Hong, S.W., 2006. A study on motion and wave drift force of a BBDB type OWC wave energy device. *Journal of Ocean Engineering and Technology*, 20(2), pp.22-28.

Kim, J.H., Lew, J.H., Hong, D.C., Kim, Y.S., Choi, H.S. and Hong, S.W., 2007. A study on motion of a BBDB type OWC wave energy device considering pneumatic damping coefficients in the duct. *Proceedings of 17th International Offshore and Polar Engineering Conference*, ISOPE, Lisbon, Portugal, 1-6 July 2007, pp.483-488.

Koo, W.C. and Kim, M.H., 2004. Freely floating-body simulation by a 2D fully nonlinear numerical wave tank. *Ocean Engineering*, 31(16), pp.2011-2046.

Koo, W.C. and Kim, M.H., 2010. A nonlinear time-domain simulation of a land-based oscillating water column. *Journal of Waterway, Port, Coastal and Ocean Engineering,* 136(5), pp.276-285.

Koo, W.C. and Lee, K.R., 2011. Numerical and experimental analysis of Backward Bent Duct Buoy (BBDB) wave energy converter. *Proceedings of the 21st International Offshore and Polar Engineering Conference*, ISOPE, Hawaii, USA, 19-24 June 2011, pp.655-660.

Koo, W.C., Kim, S.J. and Kim, M.H., 2012. Numerical analysis of a floating wave energy converter, Backward Bent Duct Buoy (BBDB) with different shaped-corners. *Proceedings of 31st International Conference on Ocean, Offshore and Arctic Engineering*, OMAE-83666, Rio de Janeiro, Brazil. 1-6 July 2012, pp.669-674.

Masuda, Y., 1971. Wave activated generator. *Proceedings of International Colloquium on Exposition of the Oceans*, Bordeaux, France, March.

Masuda, Y., Yamazaki, T., Outa, Y. and McCormick, M.E., 1987. Study of backward bent duct buoy. *Proceedings of Oceans '87*, IEEE, 19, pp.384-389.

McCormick, M. and Sheehan, W., 1992. Positive drift of a backward-bent duct barge. *Journal of Waterway, Port, Coastal, and Ocean Engineering*, 118(1), pp.106-111.

McCormick, M.E., 2007. *Ocean wave energycConversion.* Dover Publication.

Nagata, S., Toyota, K., Imai, Y. and Setoguchi, T., 2008. Experimental study on hydrodynamic forces acting on a floating wave energy converter 'Backward Bent Duct Buoy'. *Proceedings of 18th International Offshore and Polar Engineering Conference*, ISOPE, Vancouver, BC, Canada, 6-11 July 2008, pp.366-373.

Nagata, S., Toyota, K., Imai, Y. and Setoguchi, T., 2009. Numerical simulation for evaluating of primary energy conversion of floating OWC-type wave energy converter. *Proceedings of 19th International Offshore and Polar Engineering Conference*, ISOPE, Osaka, Japan, 21-26 June 2009, pp.300-307.

Park, M., Koo, W. and Choi, Y., 2010. Hydrodynamic interaction with an array of porous circular cylinders. *International Journal of Naval Architecture and Ocean Engineering*, 2(3), pp.146-154.

Sarmento, A. and Falcão, A.F.O., 1985. Wave generation by an oscillating surface-pressure and its application in wave-energy extraction. *Journal of Fluid Mechanics,* 150, pp.467-485.

Suzuki, M. and Arakawa, C., 2000. Guide vanes effects of wells turbine for wave power generator. *International Journal of Offshore and Polar Engineering*, 10 (2), pp.153-159.

Suzuki, M., Kuboki, T., Nagata, S. and Setoguchi, T., 2011. Numerical investigation of 2D optimal profile of backward-bent duct type wave energy converter. *Journal of Offshore Mechanics and Arctic Engineering*, 133, pp.041602-1.

Tanizawa, K. and Naito, S., 1997. A study on parametric roll motions by fully nonlinear numerical wave tank. *Proceedings of 7th International Offshore and Polar Engineering Conference*, ISOPE, Honolulu, USA, 3, 25-30 May 1997, pp.69-75.

Toyota, K., Nagata, S., Imai, Y. and Setoguchi, T., 2008. Effects of hull shape on primary conversion characteristics of a floating OWC 'Backward Bent Duct Buoy'. *Journal of Fluid Science and Technology*, 3(3), pp.458-465.

Toyota, K., Nagata, S., Imai, Y. and Setoguchi, T., 2009. Research for evaluating performance of OWC-type wave energy converter 'Backward Bent Duct Buoy'. *Proceedings of 8th European Wave and Tidal Energy Conference*, Uppsala, Sweden, 7-10 September 2009, pp.901-913.

Toyota, K., Nagata, S., Imai, Y., Oda, J. and Setoguchi, T., 2010. Primary energy conversion characteristics of a floating OWC 'Backward Bent Duct Buoy'. *Proceedings of 20th International Offshore and Polar Engineering Conference*, ISOPE, Beijing, China, 20-26 June 2010, pp.850-855.

Vinje, T. and Brevig, P., 1981. Numerical simulation of breaking wave. *Advances in Water Resources*, 4(2), pp.77-82.

Wang, D.J., Katory, M. and Li, Y.S., 2002. Analytical and experimental investigation on the hydrodynamic performance of onshore wave-power devices. *Ocean Engineering*, 29(8), pp.871-885.